Appendix for Chapter 3

Appendix 3.1 Brief overview of the Jahn Teller (JT) effect

The original Jahn Teller (JT) theorem (1934) states that a *non-linear* molecule in a degenerate electronic orbital state distorts to a lower symmetry configuration to remove the degeneracy.[1] The theorem was extended to *linear* molecules for quadratic or second order vibronic coupling terms by Renner and Teller (Renner-Teller effect) and to molecules with near degenerate states by Öpik and Pryce (pseudo-JT effect).[2-4] Proof of the JT theorem involves perturbation theory, in which the corrections terms are the Taylor expanded vibronic coupling terms.

We define the Hamiltonian as the sum of the electronic potential (H_{electr}) for the system at its symmetric configuration (0 subscript in the formulas), the kinetic energy of the nuclei (T_{nuclr}), the electrostatic potential of the system ($V(r,Q)$) as a function of both nuclear (Q) and electronic (r) coordinates, and the spin-orbit Hamiltonian (H_{so}):

$$H = H_{electr} + T_{nuclr} + V(r,Q) + H_{SO} \qquad \text{(A-3.1)}$$

with $$V(r,Q) - V(r,0) = \sum_i^N (\frac{\partial V}{\partial Q_i})_0 Q_i + \frac{1}{2}\sum_{i,j}^N (\frac{\partial^2 V}{\partial Q_i \partial Q_j})_0 Q_i Q_j + \ldots \qquad \text{(A-3.2)}$$

The H_{SO} term is typically included, as JT systems necessarily involve open-shell systems. Both vibrational and spin angular momenta compete for the orbital angular momentum. In the case of NO_3, the spin-orbit coupling term is expected to be very small compared to the JT distortion. Thus, the H_{SO} term is often ignored.

Analysis of NO_3 (D_{3h}) is parallel to Barckholtz and Miller's analysis of a C_{3v} molecule in a ^2E state with degenerate JT active mode $Q_{i,\pm}(e)$. Using vibronic basis set $\{|\Lambda\rangle\prod|v_i,l_i\rangle\}$, the eigenvalues for the Hamiltonian are:[5]

$$U_{i,\pm} = \frac{1}{2}\lambda_i\rho_i^2 \pm \rho_i k_i(1+\frac{2g_{ii}\rho_i}{k_i}\cos(3\phi_i)+\frac{g_{ii}^{\ 2}\rho_i^{\ 2}}{k_i^{\ 2}})^{\frac{1}{2}}$$
$$\sim \frac{1}{2}\lambda_i\rho_i^2 \pm [k_i\rho_i + g_{ii}\rho_i^{\ 2}\cos(3\phi_i)] \qquad \text{(A-3.3)}$$

with λ_i = curvature of the potential energy surface at the symmetric configuration, k_i = linear JT constant, and g_{ii} = quadratic JT constant.

$$Q_{i,\pm} = \rho_i e^{\pm i\phi_i} \qquad \text{(A-3.4)}$$

$$\lambda_i = \langle\Lambda|(\frac{\partial^2 V}{\partial Q_{i,+}\partial Q_{i,-}})_0|\Lambda\rangle \qquad \text{(A-3.5)}$$

$$k_i = \langle\Lambda|(\frac{\partial V}{\partial Q_{i,\pm}})_0|-\Lambda\rangle \qquad \text{(A-3.6)}$$

$$g_{ii} = \langle\Lambda|(\frac{\partial^2 V}{\partial Q_{i,\pm}^{\ 2}})_0|-\Lambda\rangle\,. \qquad \text{(A-3.7)}$$

The minimum and maximum energies at $\phi_{\min,i} = 0, \frac{2\pi}{3}, \frac{4\pi}{3}, \ldots$ and $\phi_{\max,i} = \frac{\pi}{3}, \pi, \ldots$ are:

$$E_{\min/\max,i} = -D_i\omega_{e,i}(1\pm K_i)\,, \qquad \text{(A-3.8)}$$

where M_i = reduced mass of the JT active mode and

$$D_i = \frac{k_i^2}{2\hbar}\left(\frac{M_i}{\lambda_i^3}\right)^{\frac{1}{2}} \qquad \text{(A-3.9)}$$

$$K_i = \frac{g_{ii}}{\lambda_i} \qquad \text{(A-3.10)}$$

From equation A-3.8, distortion to lower symmetry occurs only when the linear JT or first order vibronic coupling term is non-zero ($D_i \neq 0$). The quadratic JT term ($K_i \neq 0$) removes the symmetry of the distortion. In literature, the JT stabilization energy is often reported as $\varepsilon = |E_{min/max,i}|$ with $K_i = 0$. The expression for the PJT effect is mathematically equivalent to the linear JT term. Both JT and PJT effects are needed to describe distortions in NO_3.

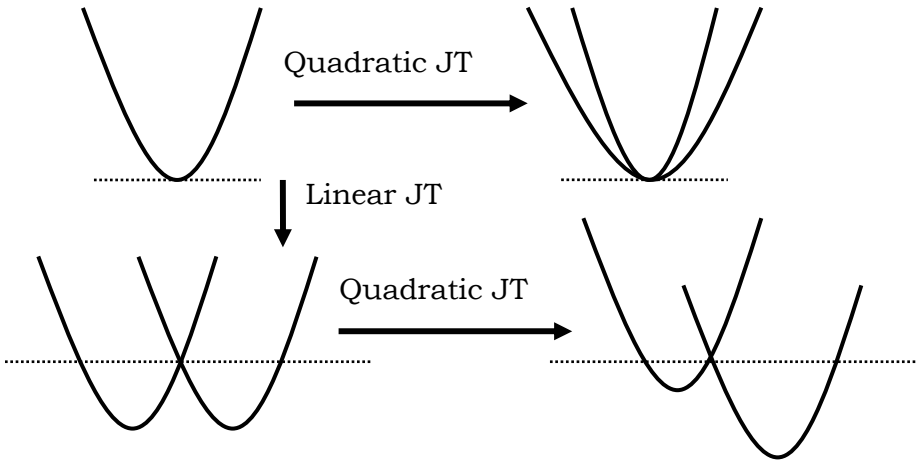

Figure A-3.1. Schematics of a two-dimensional slice of a potential energy surface with linear and quadratic JT effects. The linear JT effect must be non-zero for the system to undergo distortion.

Appendix 3.2 Results from our previous CRDS study

In our previous CRDS study, we examined the Herzberg-Teller-allowed $\tilde{A} \leftarrow \tilde{X}$ transitions of NO_3 in the 5000-10000 cm^{-1} region at room temperature.[6,7] The D_{3h} and C_{2v} character tables, along with a correlation table, are shown in Fig. A-3.2. Assuming D_{3h} symmetry, we access all vibrational levels of the $\tilde{A}$ state, except the υ_1' level, from the ground state. Given the perpendicular and parallel electric dipole transition moments $\mu_\perp = E'$ and $\mu_\parallel = A_2''$, the transitions are the following:

$$
\begin{aligned}
1_0^1 &: a_1' \notin A_2' \otimes (E' \oplus A_2'') \otimes (E'' \otimes a_1') \\
2_0^1 &: a_1' \in A_2' \otimes (E') \otimes (E'' \otimes a_2'') \\
3_0^1 &: a_1' \in A_2' \otimes (A_2'') \otimes (E'' \otimes e') \\
4_0^1 &: a_1' \in A_2' \otimes (A_2'') \otimes (E'' \otimes e')
\end{aligned}
\qquad \text{(A-3.11)}
$$

The listed bands, along with multiple combination bands, were identified in the previous study. Assignments can be found in the original published papers.

D_{3h}	E	$2C_3$	$3C_2$	σ_h	$2S_3$	$3\sigma_v$		
A_1'	1	1	1	1	1	1		x^2+y^2, z^2
A_1'	1	1	-1	1	1	-1	R_z	
E′	2	-1	0	2	-1	0	(x,y)	(x^2-y^2, xy)
A_1''	1	1	1	-1	-1	-1		
A_2''	1	1	-1	-1	-1	1	z	
E″	2	-1	0	-2	1	0	(R_x, R_y)	(xz, yz)

C_{2v}	E	C_2	$\sigma_v(xz)$	$\sigma_v'(yz)$		
A_1	1	1	1	1	z	x^2, y^2, z^2
A_2	1	1	-1	-1	R_z	xy
B_1	1	-1	1	-1	x, R_y	xz
B_2	1	-1	-1	1	y, R_x	yz

D_3	C_{2v}
A_1'	A_1
A_1'	B_2
E'	A_1+B_2
A_1''	A_2
	B_1
A_2''	$A_2 + B_1$

Figure A-3.2. The D_{3h} (top) and C_{2v} [8] character tables. The correlation table is also included on the side.

The parallel 4_0^1 and perpendicular 2_0^1 bands are shown in Fig. A-3.3. While the rotational contours of the bands are distinct, the two bands have surprisingly similar intensities. The rotational contours are discussed in Appendix 3.5. We focus here on the intensities of the two bands. Examination of the intensity borrowing mechanisms reveals the importance of the PJT effect in NO_3. (Fig. A-3.4).[9]

For the 4_0^1 band, the wavefunction describing the ground state of NO_3 has contributions from both the $\tilde{X}$ and $\tilde{B}$ states:

$$|\Psi,\tilde{X}\rangle = |\tilde{X}\rangle + \lambda_{PJT:BX}\,|\tilde{B},e'\rangle \qquad \text{(A-3.12 a)}$$

where $\lambda_{PJT:BX}$ = PJT coupling between the $\tilde{X}$ and $\tilde{B}$ states. The transition dipole moment for the 4_0^1 band is then:

$$\langle\Psi,\tilde{X}\,|\,\mu_{\|}\,|\,\tilde{A},e'\rangle = \langle\tilde{X}\,|\,\mu_{\|}\,|\,\tilde{A},e'\rangle + \lambda_{PJT:BX}\langle\tilde{B},e'\,|\,\mu_{\|}\,|\,\tilde{A},e'\rangle\,. \qquad \text{(A-3.12 b)}$$

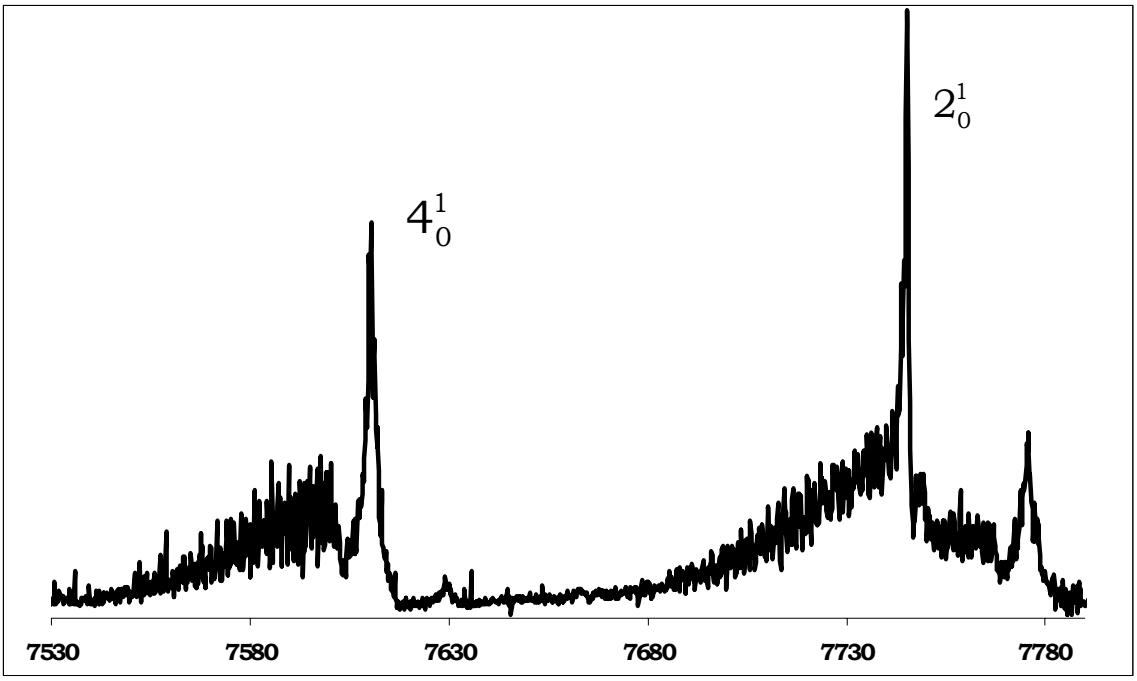

Figure A-3.3. CRD spectrum of the 4_0^1 and 2_0^1 bands in the 7530-7800 cm^{-1} region.

For the 2_0^1 band, the wavefunction describing the $\tilde{A}$ state has contributions from both the $\tilde{A}$ and $\tilde{B}$ states:

$$|\Psi, \tilde{A}, a_2''\rangle = |\tilde{A}, a_2''\rangle + \lambda_{PJT:AB} |\tilde{B}\rangle \qquad \text{(A-3.13 a)}$$

where $\lambda_{PJT:AB}$ = PJT coupling between the $\tilde{A}$ and $\tilde{B}$ states. The transition dipole moment for the band is then:

$$\langle \tilde{X} | \mu_\perp | \Psi, \tilde{A}, a_2''\rangle = \langle \tilde{X} | \mu_\perp | \tilde{A}, a_2''\rangle + \lambda_{PJT:AB} \langle \tilde{X} | \mu_\perp | \tilde{B}\rangle \qquad \text{(A-3.13 b)}$$

For the 4_0^1 band, $\lambda_{PJT:BX}$ is expected to be very strong, while for the 2_0^1 band, the $\tilde{B} \leftarrow \tilde{X}$ transition is known to be very strong. Thus, the 4_0^1 and 2_0^1 bands coincidentally have similar intensities. From our simulations

of the experimental data, the intensity ratio of the bands $2_0^1 : 4_0^1$ was 1.76. Stanton modeled the intensities using a linear multimode vibronic coupling (LVC) model and found the ratio to be 1.36.[9]

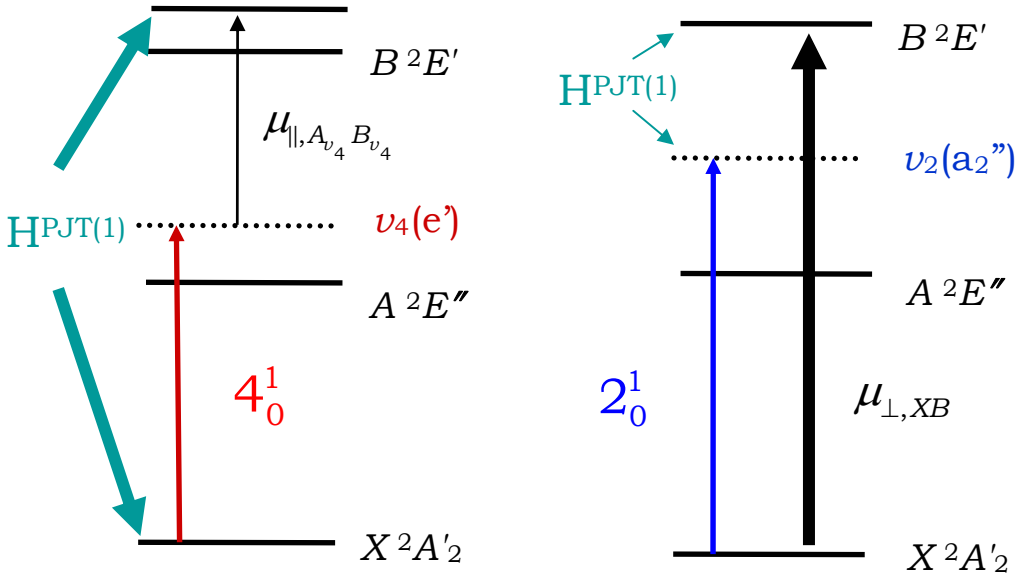

Figure A-3.4. Schematics of the intensity borrowing mechanisms for the parallel 4_0^1 and perpendicular 2_0^1 bands of NO_3. The parallel band borrows intensity from the weak $\tilde{B} \leftarrow \tilde{A}$ transition via strong PJT coupling between the $\tilde{B}$ and $\tilde{X}$ states. The perpendicular band borrows intensity from the strong $\tilde{B} \leftarrow \tilde{X}$ band via weak PJT coupling between the $\tilde{A}$ and $\tilde{B}$ states.

The analysis of the bands highlighted the importance of the PJT effect in NO_3. However, an interesting puzzle arose during the simulations. A symmetric top model was used to simulate the 4_0^1 band; however an asymmetric top model had to be used to simulate the 2_0^1 band. Asymmetry indicates JT distortion. What is then the symmetry or the extent of vibronic coupling in the 0^0 level of the $\tilde{A}$ state?

Detection of the origin band 0_0^0 would solve the puzzle. The $\tilde{A} \leftarrow \tilde{X}$ transition is electric dipole forbidden; however the origin band 0_0^0 is magnetic-dipole and electric-quadrupole-allowed:

D_{3h} :

magnetic $0_0^0 : a_1' \in A_2' \otimes (\cancel{a_2'} \oplus e'') \otimes E''$

electric quadrupole $0_0^0 : a_1' \in A_2' \otimes (\cancel{a_1'} \oplus \cancel{e'} \oplus e'') \otimes E''$

(A-3.14)

C_{2v} :

magnetic $0_0^0 : a_1 \in B_2 \otimes (\cancel{b_1} \oplus \cancel{b_2} \oplus a_2) \otimes B_1$

electric quadrupole $0_0^0 : a_1 \in B_2 \otimes (\cancel{b_1} \oplus \cancel{b_2} \oplus \cancel{a_1} \oplus a_2) \otimes B_1$

The absorptions are expected to be very weak. A better NO_3 source would be necessary to increase the signal-to-noise of the spectra. Thus Chapter 3 built on the previous CRDS study by focusing on detection of the origin band and the hot bands in the 7000-7600 cm^{-1} region.

Appendix 3.3 N_2O_5 synthesis

Dinitrogen pentaoxide (N_2O_5) is synthesized in the hood by mixing gases, nitric oxide NO and ozone O_3, in a glass vessel (Fig A-3.5). The gas product N_2O_5 is collected in a bubbler in a dry ice/acetone bath. The product is a white powder or crystal. N_2O_4 impurities can easily be observed by a slight yellow tinge to the powder. To remove impurities, lift the bubbler out of the dry ice/acetone bath and run ozone through the bubbler until the yellow color disappears.

N_2O_5 crystals will form on any cold surface, including the inner tube of the bubbler. Before running experiments, warm the sample slowly by running either ozone or helium at room temperature through the bubler. Shake the bubbler gently to push all the N_2O_5 sample into the bottom of the bubbler. If extra N_2O_5 is synthesized, the bubbler can be put under high pressure helium and placed in liquid nitrogen for storage. Proper care should be taken when handling liquid nitrogen (Appendix 2.4).

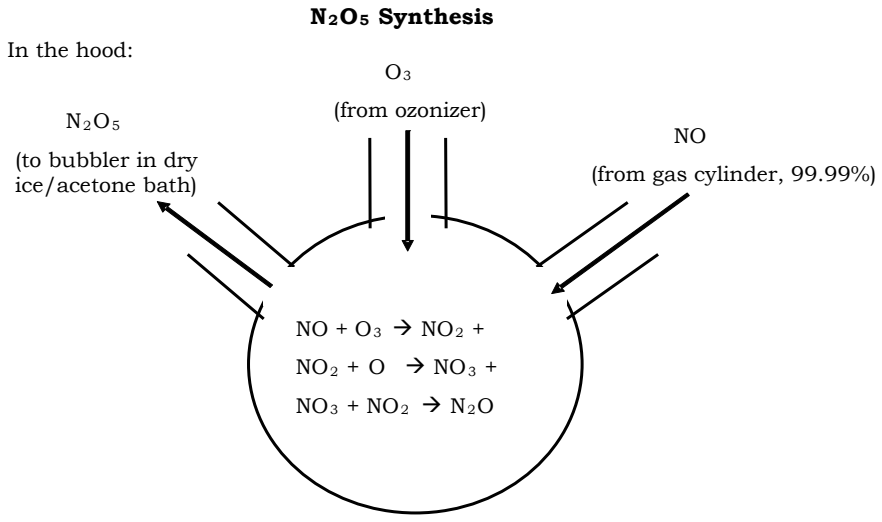

Figure A-3.5. Schematic of the synthesis of N_2O_5. All connections should be vacuum tight and made from stainless steel or Teflon, as ozone and nitric oxide destroy most o-rings.

Appendix. 3.4 Nitric acid absorption in the NIR region

The overtone and combination bands of nitric acid (HNO_3) have been examined for potential contributions to the photochemistry of the atmosphere.[10,11] We further explored HNO_3 absorptions in the NIR region using the pulsed CRDS apparatus. Details of the pulsed CRDS apparatus has been provided in Chapter 2. The Nd:YAG was operated at 20 Hz for maximum data collection per second.

To minimize water absorptions in the NIR, we prepared a 3:1 solution of sulfuric acid (concentrated) and nitric acid (70% HNO_3) in a bubbler. The sample was freeze-pump-thawed before being placed in an ice bath. Helium (~20 Torr) was flowed slowly over the HNO_3 bubbler (P_{vapor} ~ 1.5 Torr) and into a long residence time Pyrex ringdown cell. The ringdown cell was wrapped with thermal tape for temperature experiments.

Preliminary spectra were collected from 7200-7600 cm^{-1} and 7900-8300 cm^{-1} at 0.2 cm^{-1} step size at both T = 25˚C and T = 60˚C. The absorption features were identical at both temperatures, thus only the preliminary spectra of nitric acid at room temperature are shown in Fig. A-3.6 (a-b).

The HNO_3 bands are surprisingly structured in the region. Calculated intensities of the bands have been plotted in Fig. A-3.6 (a).[12] The experimental and theoretical data match very well. The strong OH overtone at ~6940 cm^{-1} has been well-studied, with measured absorption cross section $\sigma < 6.9 \times 10^{-19}$ cm^2 cm^{-1} $molec^{-1}$.[12,13] CRDS, however, cannot quantitatively measure strong absorptions (Chapter 2). We therefore are currently in the process of diluting HNO_3 concentrations such that spectra of both the OH overtone and combination bands can be obtained simultaneously. The integrated intensities of the bands can then be directly compared.

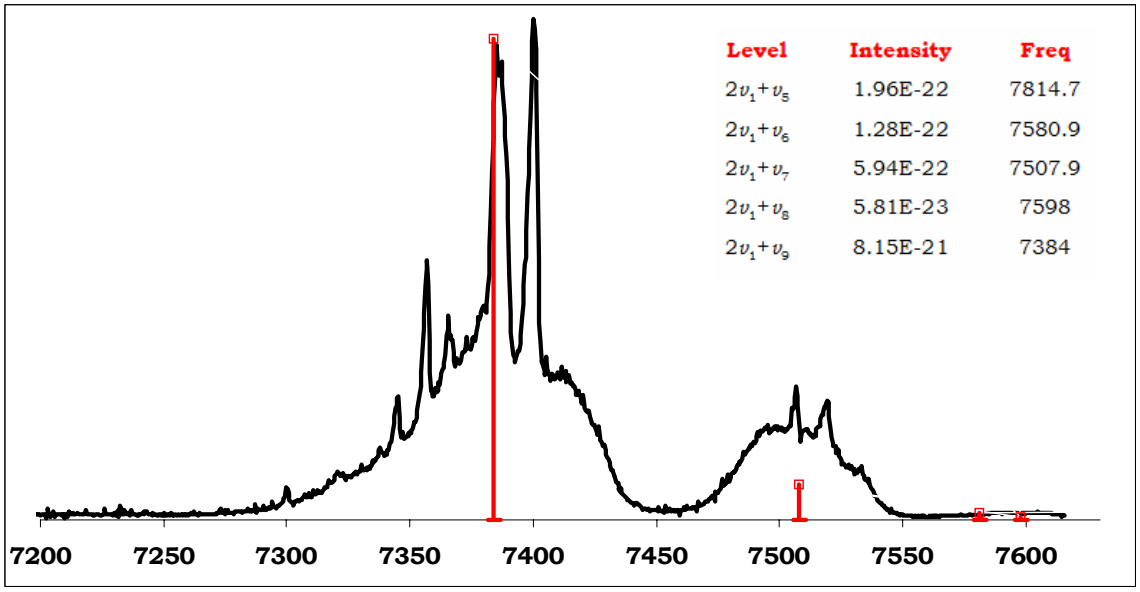

Figure A-3.6 (a). CRD spectrum of nitric acid in the 7200-7650 cm^{-1} NIR region. The red lines are from VPT2 calculations from ref [11].

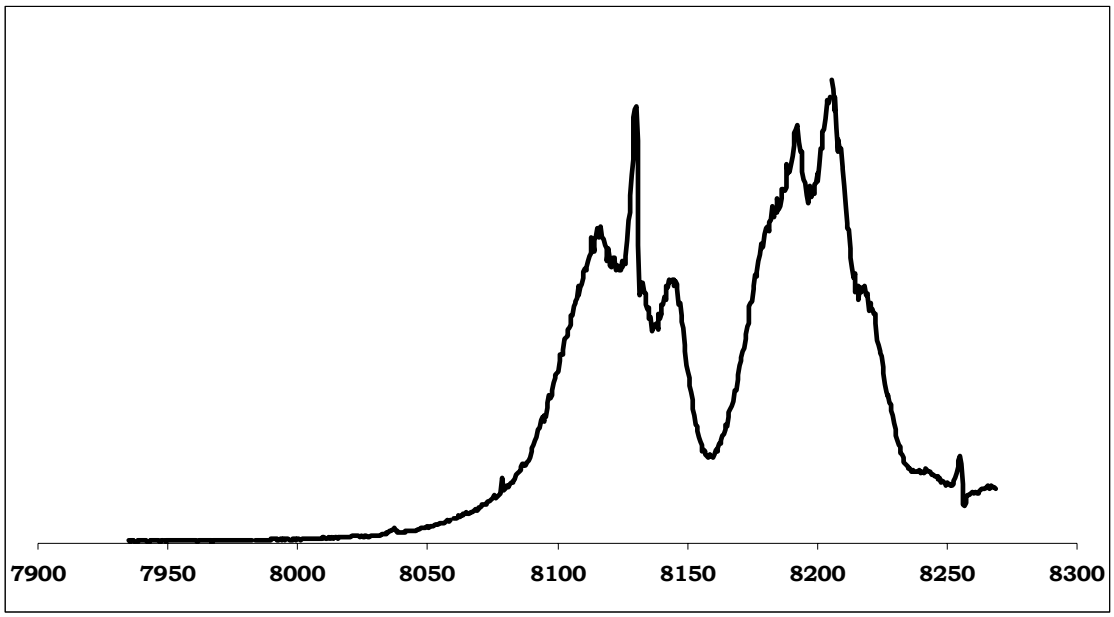

Figure A-3.6 (b). CRD spectrum of nitric acid in the 7900-8500 cm^{-1} NIR region.

Appendix 3.5 Calculations and simulations of NO_3

A-3.5.1. PGopher simulations

We simulated the rotational contours of the NO_3 bands using PGopher v. 5.3. In Appendix 3.2, we compared the intensities of the parallel 4_0^1 and perpendicular 2_0^1 bands. We began simulations with these bands (Fig. A-3.7 and Fig. A-3.8). A comparison of the contours shows that the 4_0^1 band has a small gap, caused by shifting of the Q-branch to the blue of the bandhead. The distinct contours for perpendicular and parallel bands are useful for band assignments in NO_3.

We next simulated the observed hot bands in the 7000-7600 cm^{-1} region. In a recent study, Kawaguchi, *et al.* fit the $\upsilon_3 + \upsilon_4 \leftarrow \upsilon_4$ and $\upsilon_3 + 2\upsilon_4 \leftarrow \upsilon_4$ bands in the ground state to determine the rotational constants of the 4_1 level.[14] We used these values to model the transitions; however, simulations were still difficult, as the observed bands consisted of a convolution of multiple hot bands in some absorption regions.

In the 7300-7400 cm^{-1} region, we used the upper rotational constants of the 2_0^1 band to simulate the $4_1^0 2_0^1$ band (Fig. A-3.9). There may be a second peak at 7360 cm^{-1}. If we adjust C′, however, the simulation matches the rotational contour of the hot band. Thus, we assigned the band origin of the $4_1^0 2_0^1$ band with large error bars to 7370.0(3.0) cm^{-1}. We analyzed the hot bands in the 7200-7270 cm^{-1} and 7450-7500 cm^{-1} regions similarly and assigned the peaks to 4_1^1 at 7235.5(1.5) cm^{-1} and $4_1^0 1_0^1$ at 7481.0(1.0) cm^{-1}, respectively (Fig. A-3.10 and A-3.11).

Simulation of the 0_0^0 origin band was the most difficult (Fig. A-3.12). We could not re-create the two peaks with a magnetic dipole model. We therefore fit the first peak to the magnetic dipole transition and simulated perpendicular and parallel bands to take into account the other absorption features in the 7000-7100 cm^{-1} region. In order to check whether the rotational constants for the 0^0 level were reasonable, we used the same rotational constants to fit the 4_1^0 band (Fig. A-3.13). The simulated contour was in good agreement with the experimental 4_1^0 band.

We also tried using an electric quadrupole model to fit the absorption peaks (Fig. A-3.14), but this model also could not recreate the two absorption features. Electric quadrupole transitions are much weaker than magnetic dipole transitions; thus we maintain that the observed features resulted from the 0_0^0 magnetic dipole transition. Determination of υ_4'' = 365.75(1.1) cm^{-1} from $0_0^0 - 4_1^0$ are very consistent with previous measurements of the υ_4'' level (υ_4'' = 365.6 cm^{-1} and 365.48419 cm^{-1}).[14,15] Thus, we used the magnetic dipole PGopher simulation of the 0_0^0 band to calculate the integrated absorption cross section in the study.

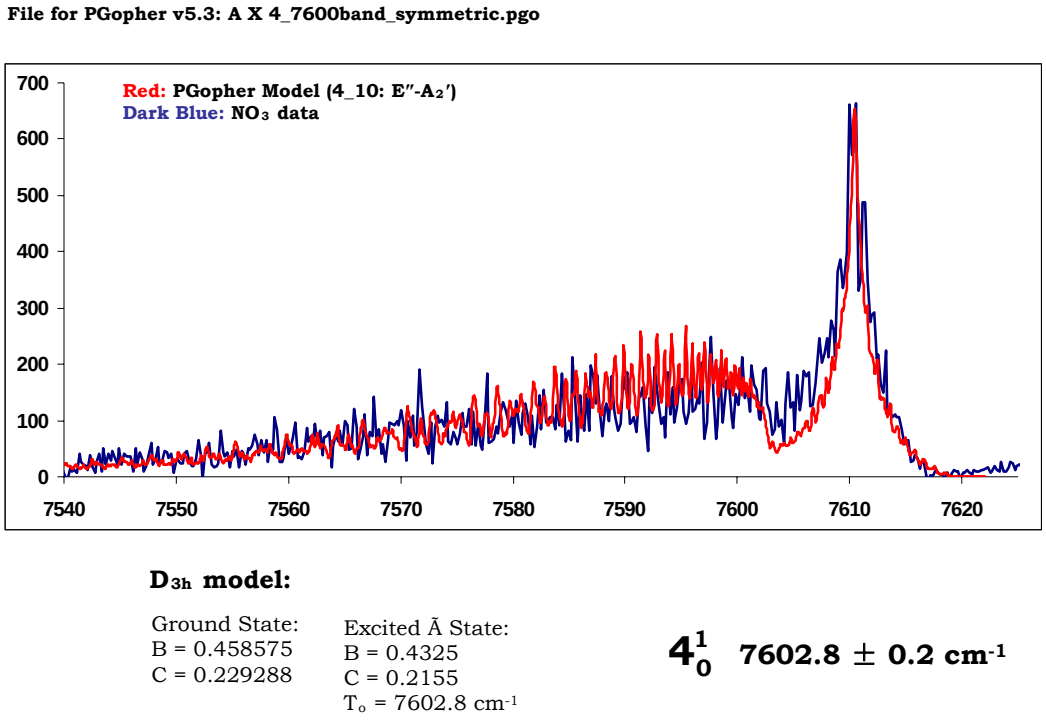

Figure. A-3.7. PGopher simulation of the 4_0^1 band using a symmetric top model.

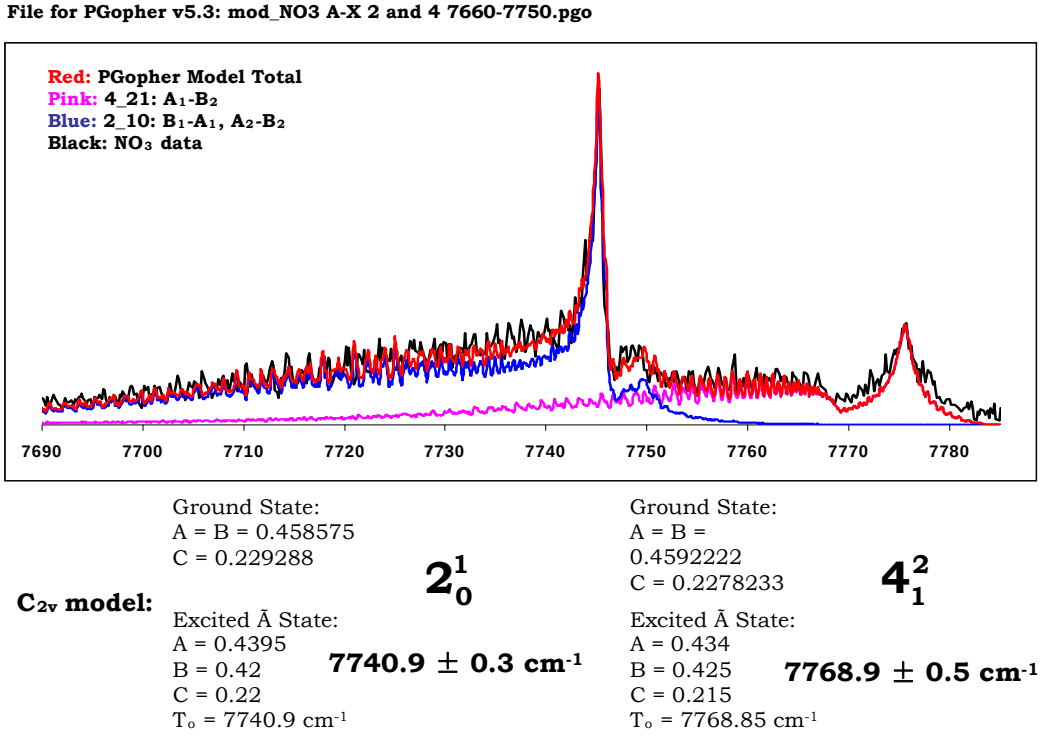

Figure A-3.8. PGopher simulation of the 2_0^1 band using a symmetric top model.

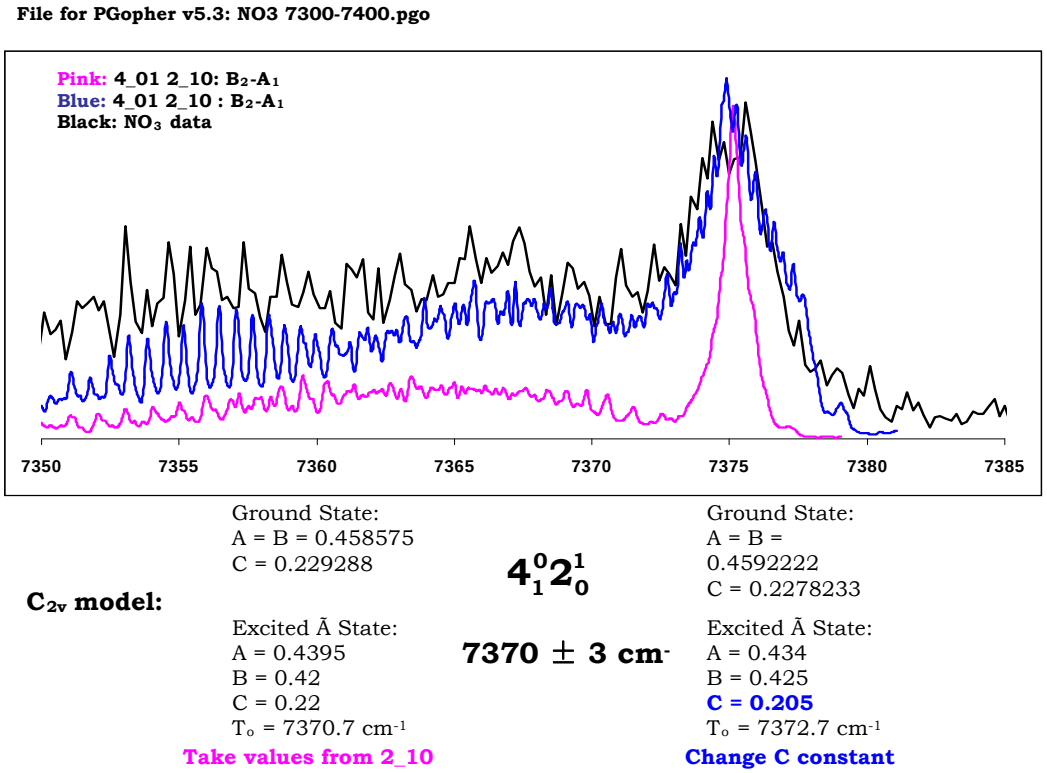

Figure A-3.9. PGopher simulation of the $4_1^0 2_0^1$ band using an asymmetric top model.

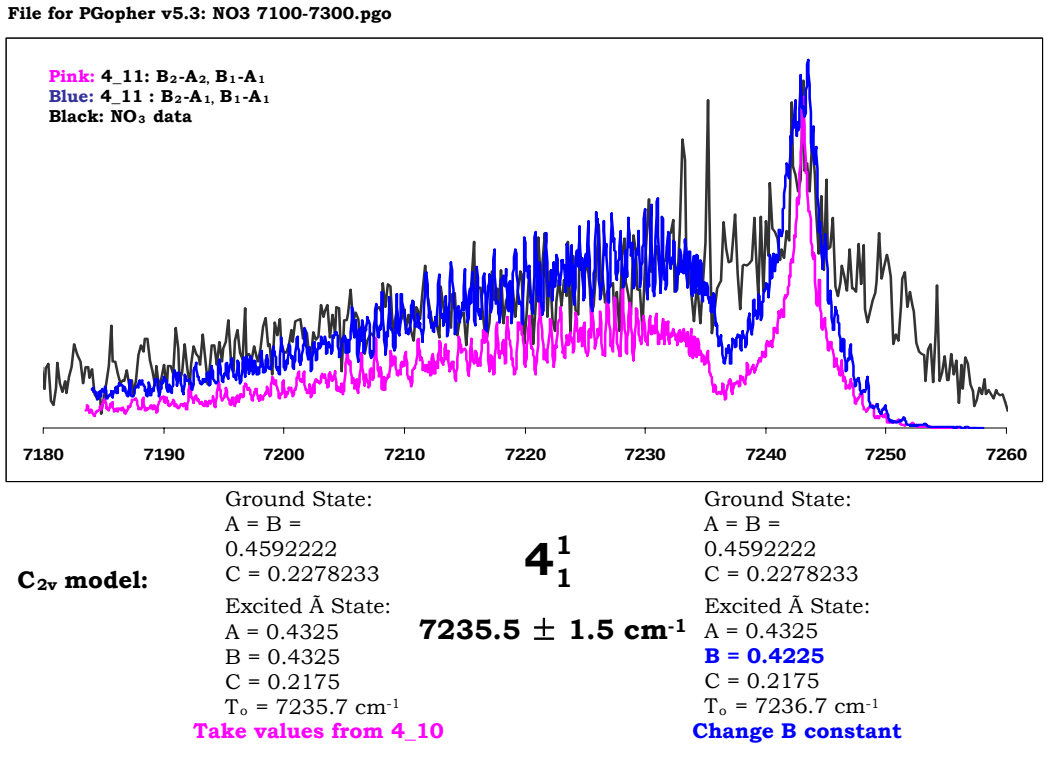

Figure A-3.10. PGopher simulation of the 4_1^1 band using an asymmetric top model.

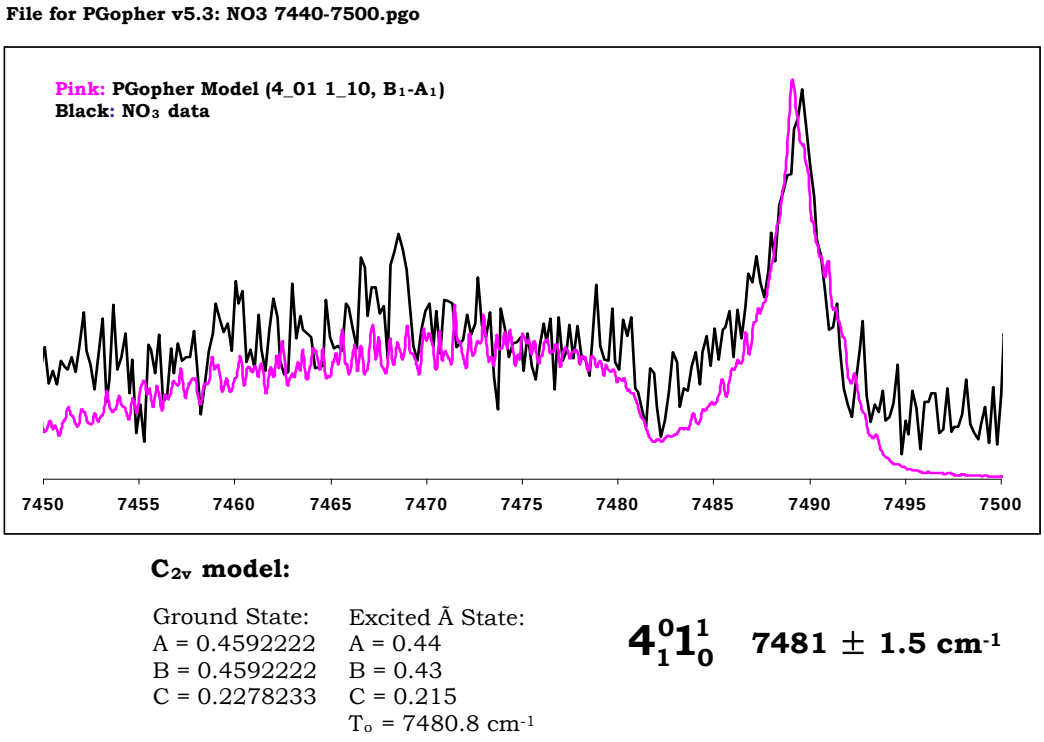

Figure A-3.11. PGopher simulation of the $4_1^0 1_0^1$ band using an asymmetric top model.

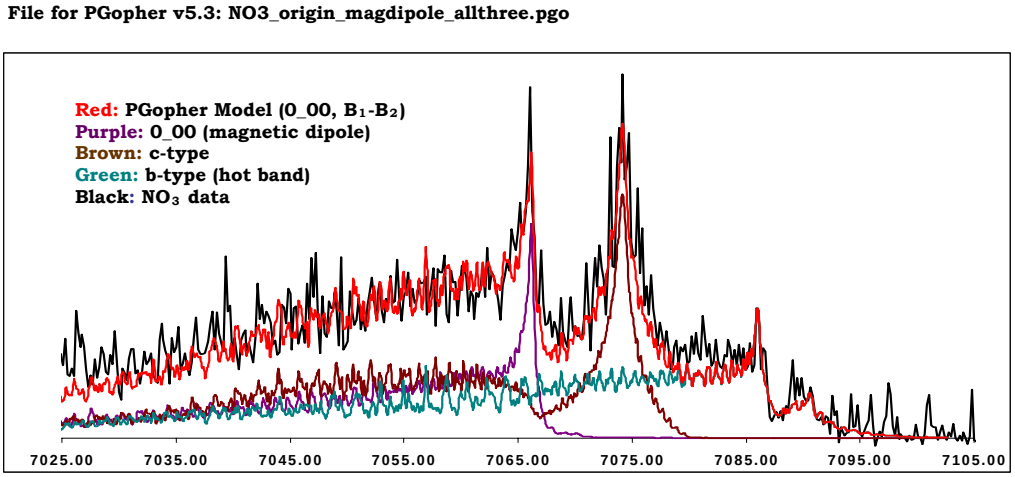

Figure A-3.12. PGopher simulation of the 0_0^0 band using a magnetic dipole C_{2v} model.

File for PGopher v5.3: 4_01_6700_ICOSband.pgo

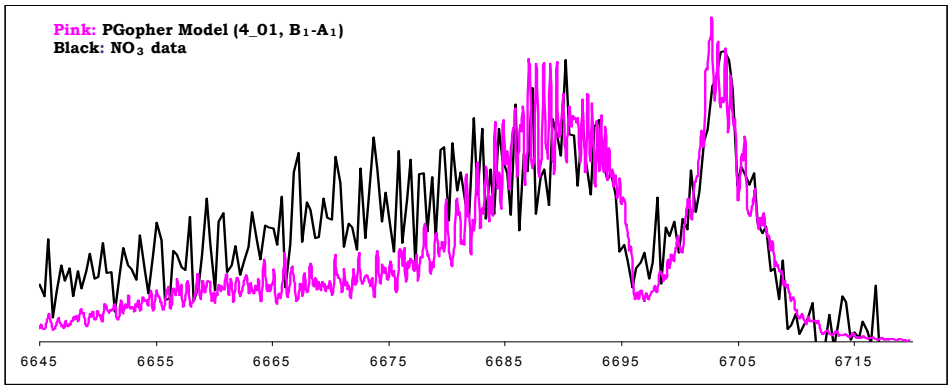

C_{2v} model:

Ground State:
A = 0.4592222
B = 0.4592222
C = 0.2278233

Excited Ã State:
A = 0.445
B = 0.4125
C = 0.2175
T_o = 6696.5 cm^{-1}

Take values from 0_00

4_1^0 **6696.5 ± 1.0 cm^{-1}**

Figure A-3.13. PGopher simulation of the 4_1^0 band using an asymmetric top model.

Electric quadrupole model

In PGopher, simulate an electric quadrupole transition by using a spherical transition moment and choosing rank 2. Components (-2, 0, 2) resulted in spectra, although all component may not be allowed in NO_3.

File for PGopher v5.3: quadrupole.pgo

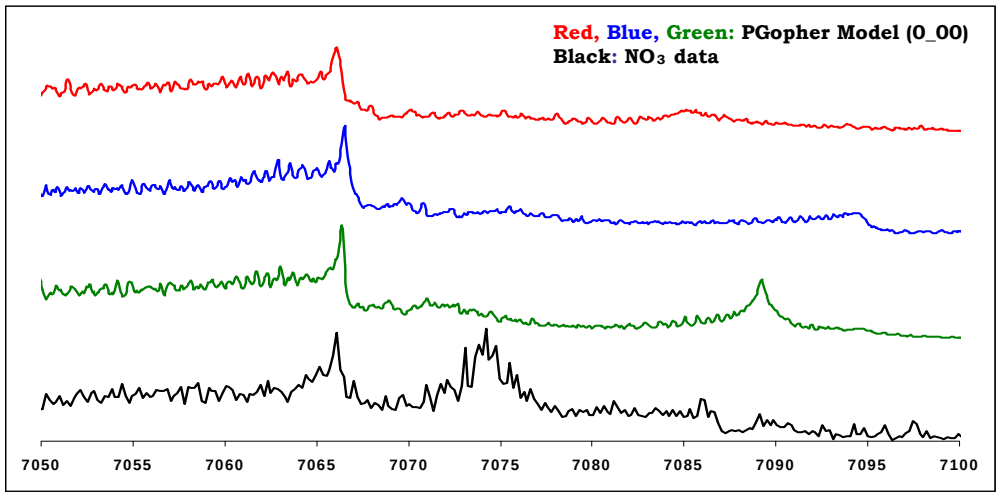

C_{2v} model: **From earlier 0_00 fit**

Ground State:	Excited Ã State:	Excited Ã State:	Excited Ã State:
A = 0.458575	A = 0.445	A = 0.445	**A = 0.435**
B = 0.458675	B = 0.4125	**B = 0.43**	**B = 0.43**
C = 0.229288	C = 0.2175	C = 0.2175	C = 0.2175
	T_o = 7062.25 cm^{-1}	T_o = 7062.25 cm^{-1}	T_o = 7062.25 cm^{-1}

Figure A-3.14. PGopher simulation of the 0_0^0 band using an electric quadrupole C_{2v} model.

A-3.5.2 Rotational constants

Most theoretical papers publish the structural parameters of the chemical system, rather than the rotational constants. For NO_3, the most three important parameters are *d* and *r*, the length of the NO bonds in Å units, and θ, the angle between the z-axis and NO bond. To calculate the rotational constants from these parameters, NO_3 is drawn on a yz-graph with the origin of the axes at the center of mass of NO_3 (Fig. A-3.15). The planarity of the radical simplifies the calculations. The moments of the inertia tensor are determined from the coordinates and masses (amu) of the atoms:

$$
\begin{aligned}
I_{xx} &= \sum (m_i y_i^2 + m_i z_i^2) = I_y + I_z \\
I_{yy} &= \sum (m_i x_i^2 + m_i z_i^2) = \sum m_i z_i^2 \\
I_{zz} &= \sum (m_i x_i^2 + m_i y_i^2) = \sum m_i y_i^2 \\
I_{xy} &= -\sum m_i x_i y_i = 0 \\
I_{xz} &= 0;\ I_{yz} = 0
\end{aligned}
\qquad \text{(A-3.15)}
$$

The rotational constants (A < B < C) are then:[16]

$$
\text{Rotational constant } (A,B,C) = \frac{16.8576314}{\text{Inertia } (I_{xx},\ I_{yy},\ I_{zz})} \qquad \text{(A-3.16)}
$$

The z-axis is generally chosen as the axis of the symmetry. The coordinate system in Fig. A-3.15 was chosen assuming C_{2v} symmetry for NO_3. If NO_3 has D_{3h} symmetry, the coordinate system should be rewritten such that the z-axis is coming out of the plane. The calculations simplify even further as A = B for an oblate symmetric top.

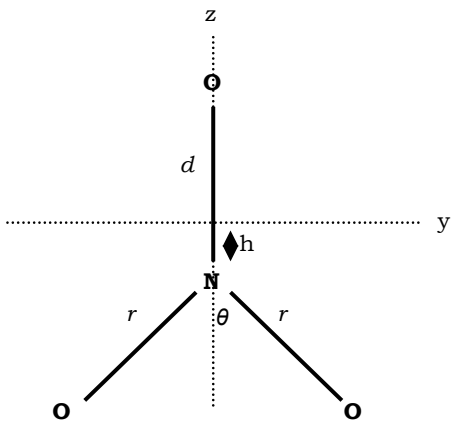

Figure A-3.15. The structural parameters of NO_3

A program was written in Mathematica to simplify the calculations. A copy of the code is provided below. Comments have been written in red to guide the reader through the program.

```
Clear[h]
mN = 14; amu
mO = 16; amu
r=1.28; angstroms
d=1.24; angstroms
θ=(120/2)*π/180; radians
Solve[mN*{0,0,-h}+mO*{0,0,d-h}
    +mO*{0,-r*Sin[θ],-h-r*Cos[θ]}+mO*{0,r*Sin[θ],-h-
r*Cos[θ]}==0,h]; solve for the center of mass of the
coordinate system i.e. h.
Ixx = mN*h^2+mO*(d-h)^2+2*mO*((-r*Sin[θ])^2+(-h-
r*Cos[θ])^2)/.Solve[mN*{0,0,-h}+mO*{0,0,d-h}
      +mO*{0,-r*Sin[θ],-h-r*Cos[θ]}+mO*{0,r*Sin[θ],-h-
r*Cos[θ]}==0,h];
Ixy=0;
Iyy=mN*h^2+mO*(d-h)^2+2*mO*(-h-r*Cos[θ])^2/.Solve[mN*{0,0,-
h}+mO*{0,0,d-h}
      +mO*{0,-r*Sin[θ],-h-r*Cos[θ]}+mO*{0,r*Sin[θ],-h-
r*Cos[θ]}==0,h];
Iyz=0;
Izz=2*mO*(r*Sin[θ])^2/.Solve[mN*{0,0,-h}+mO*{0,0,d-h}
      +mO*{0,-r*Sin[θ],-h-r*Cos[θ]}+mO*{0,r*Sin[θ],-h-
r*Cos[θ]}==0,h];
Inertia={Ixx,Iyy,Izz}
{A,B,c}=Reverse[Sort[16.8576314/Inertia]] A < B < C
```

Unfortunately, the structural parameters cannot be directly determined from the rotational constants. We can however use the relationship

between the constants to evaluate the asymmetry and non-planarity of the chemical system. For asymmetry,

$$\kappa = \frac{2B - A - C}{A - C} \tag{A-3.17}$$

Deviations from κ = 1 (oblate symmetric top) and κ = -1 (prolate symmetric top) indicate the degree of asymmetry. For non-planarity,

$$\Delta_0 = 16.8576314 \times (\frac{1}{C} - \frac{1}{A} - \frac{1}{B}) \tag{A-3.18}$$

Deviations from Δ_0 = 0 (planar) indicate non-planarity.

A-3.5.3 Simulation of the bands in Mathematica

If the Hamiltonian is well-defined, the NO_3 bands can be simulated in Mathematica. We wrote a Mathematica simulation for the 4_0^1 band using the symmetric top Hamiltonian from the high resolution diode study of the 4_0^1 band.[17] While the code is too long to include in the thesis, we outline here the ideas behind the program.

A set of quantum numbers is first chosen to describe the energy levels of the molecular system. In general, the quantum labels include *J* = the total angular momentum of the molecule *K* = the projection of *J* along the molecular *z*-axis, and *M* = the projection of *J* along a laboratory *z*-axis. It is convenient to first generate the lower and upper state energy levels separately using the Hamiltonian. The Hamiltonian is also a function of the quantum numbers and has been well-defined for symmetric tops:[16]

$$E(J,K) = BJ(J+1) - D_J(J(J+1))^2 + (A-B)K^2 - D_K K^4 - D_{JK} J(J+1)K^2$$

(A-3.19)

where D_J, D_K, D_{JK} are the centrifugal distortion constants.

The energy levels are organized by *K*-stacks, i.e., for every *K*, the *J*-dependent energy levels ($J \geq K$) for that value of *K* is calculated. Not all *J*-levels are however allowed. Thus, the symmetry of the *J*-levels must be investigated, along with the overall symmetry of the wave function describing the molecule (Chapter 3).[18]. Once the energy levels have been well-defined, for symmetric tops, the selection rules for the transition are very simple: $\Delta K = 0$, with $\Delta J = \pm 1$ for $K = 0$ and $\Delta J = 0, \pm 1$ for $K \neq 0$. A program can be written to calculate the energy differences between corresponding upper and lower energy levels from the selection rule.

A similar approach can be used for asymmetric tops. Finding good quantum numbers can be more difficult. Often the coordinate system is chosen such that the asymmetric top behaves as a near oblate or prolate symmetric top. The selection rules change according to the chosen coordinate system. Thus, great care should be taken to check that the correct selection rules are being used and the symmetry of the involved energy levels is correct within the chosen coordinate system.

The line positions are easily calculated once the Hamiltonian is well-defined. Simulating the line intensities of the bands can be more difficult. There may be some subtleties in weighing the energy levels, but to first approximation, the line intensity is a product of the square of the transition dipole moment and the Hönl-London factors. The Hönl-London factors are:[18]

For ΔK = 1,

$$P(J'') : \frac{(J''-1-K'')(J''-K'')}{J''}$$
$$Q(J'') : \frac{(J''+1+K'')(J''-K'')(2J''+1)}{4J''(J''+1)} \qquad \text{(A-3.20 a)}$$
$$R(J'') : \frac{(J''+2+K'')(J''+1+K'')}{4(J''+1)}$$

where P, Q, and R refer to ΔJ = -1, 0, and 1 respectively.

For ΔK = 0,

$$P(J'') : \frac{(J''+K'')(J''-K'')}{J''}$$
$$Q(J'') : \frac{2(J''+1)K''^2}{J''(J''+1)} \qquad \text{(A-3.20 b)}$$
$$R(J'') : \frac{(J''+1+K'')(J''+1-K'')}{(J''+1)}$$

For ΔK = -1,

$$P(J'') : \frac{(J''+1-K'')(J''+K'')(2J''+1)}{4J''(J''+1)}$$
$$Q(J'') : \frac{(J''-1+K'')(J''+K'')}{4J''} \qquad \text{(A-3.20 c)}$$
$$R(J'') : \frac{(J''+2-K'')(J''+1-K'')}{4(J''+1)}$$

For symmetric tops, only equations A-3.20 (b) are utilized. The transition dipole moment involves *ab initio* calculations that are beyond the scope

of this discussion. However for relative line intensities within the same transition, only the Hönl-London factors are needed.

Appendix 3.6 Off-axis integrated cavity output spectroscopy

The methodology of CRDS was discussed in Chapter 2. Improvements to CRDS and related cavity enhanced methods have focused on increasing the *Q*-factor of the cavity by efficiently coupling the laser to the cavity modes. In integrated cavity output spectroscopy (ICOS), the difference between the integrated light output from a cavity with and without an absorber is measured. Ideally, the spacing between the cavity modes is narrower than the laser line width such that the laser is always in resonance with the cavity.

The free spectral range (FSR) of a cavity (*L*) is defined as the frequency spacing between two successive resonant modes:

$$FSR = \Delta\upsilon_{longitudinal} = \frac{c}{2L} \qquad \text{(A-3.21)}$$

In off-axis (OA)-ICOS, the laser is aligned off-axis to the optical cavity axis such that the transverse modes are activated. The mode density of the cavity is therefore significantly increased (Fig. A-3.16).[19,20] In many cases, however, the mode spacing remains large with respect to the laser line width. Thus, either the laser or the cavity modes are modulated to randomize interaction between the laser and cavity. This can be achieved by either sweeping the laser frequencies rapidly or jittering the length of the optical cavity.

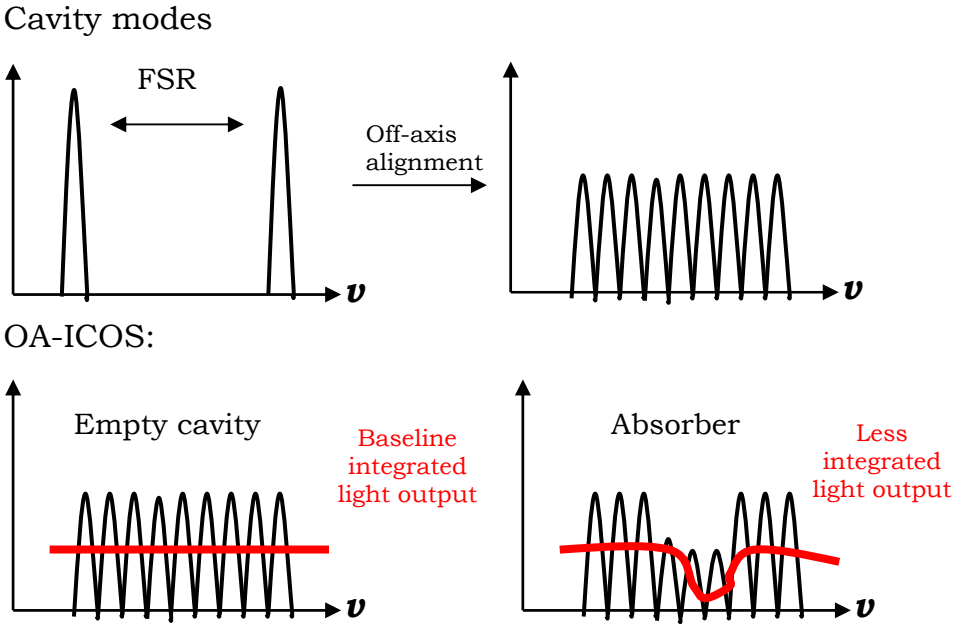

Figure A-3.16. Schematics of OA-ICOS. The integrated light output from the cavity is measured with and without an absorber. The high density of cavity modes increases the sensitivity of the method, as the baseline is better averaged.

A brief schematic of the OA-ICOS apparatus is shown in Fig. A-3.17. Output from an external cavity diode laser (New Focus TLB-6323, Γ = 100 kHz, 1407-1545 nm) with a 40-dB isolator is divided among the optical cavity, 1-m reference gas cell, and a 5-cm ultra-low expansion (ULE) quartz etalon (FSR ~ 2 GHz). A New Focus 2011 InGaAs detector (gain 10^4, BW = 50 kHz) with voltage amplifier SRS560 (30 kHz low pass filter, gain 5) and two New Focus IR 1623 detectors (BW = 50 kHz) are used for detection along their respective paths. All signals are collected using an analog-to-digital converter (Keithley Instruments, KPCI-3108) and recorded in Labview simultaneously.

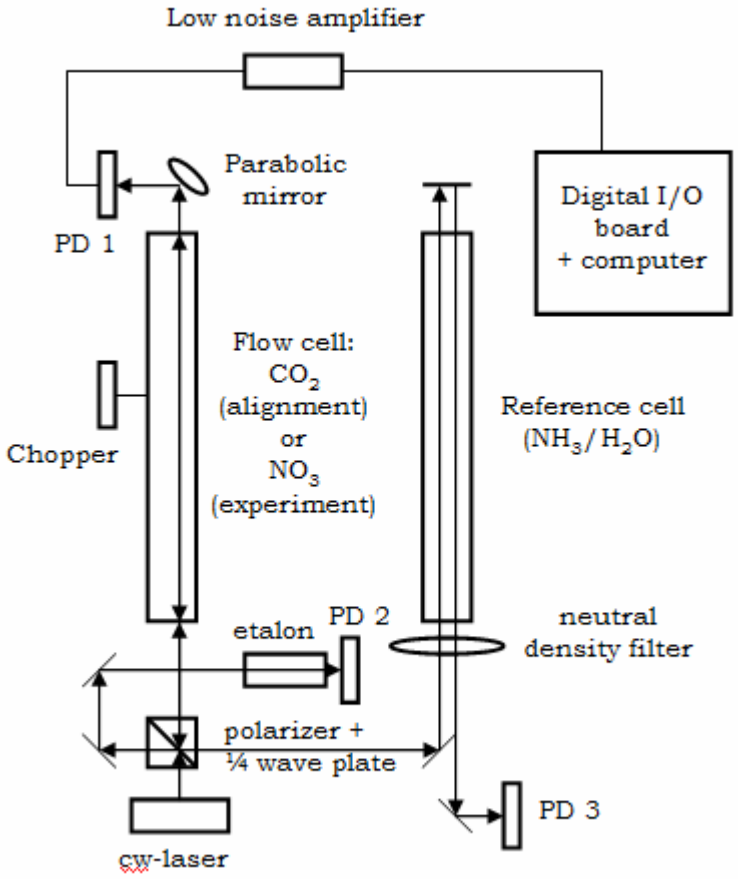

Figure A-3.17. Schematic of the OA-ICOS apparatus. The sensitivity of the apparatus is 2.5 x 10^{-8} per pass.

The optical cavity consists of two highly reflective mirrors (Newport 1500, R = 99.98%) spaced 85-cm apart (FSR ~ 176 mHz). The cavity is first aligned on-axis, before the laser is translated horizontally ~0.25 cm and tilted vertically for OA-ICOS experiments. Minor adjustments can be made while maximizing carbon dioxide signal. Mechanical jittering of the optical cavity by a chopper wheel increases the sensitivity of the apparatus to 2.5 x 10^{-8} per pass.

For the OA-ICOS experiments, the chemistry was very similar to that used in the pulsed CRDS experiment. In order to take a scan, the

piezoelectric transducer (PZT) of the laser was modulated with a 50 Hz sawtooth function to span ~1.5 cm^{-1}. The stepper motor was used to coarsely tune the wavelength of the laser such that successive PZT scans could be collected and overlapped for a global spectrum of the 4_1^0 band of NO_3. The effective resolution of the apparatus was 75 MHz or 0.002 cm^{-1}:

$$\begin{aligned} \text{resolution} &= \text{laser frequency span} \times \frac{\text{ramp frequency}}{\text{detector bandwidth}} \\ &= 45\ \text{GHz} \times \frac{50\ \text{Hz}}{30\ \text{kHz}} = 75\ \text{MHz}\ (0.002\ \text{cm}^{-1}) \end{aligned} \tag{A-3.22}$$

The resolution is sufficiently below the Doppler width of NO_3 (0.01 cm^{-1}). The reference cell was filled with either ammonia or water to provide frequency calibration, while the ULE was used to calibrate the relative spacing between the cavity modes.

The raw data is shown in Fig. A-3.18. We found however that the NO_3 concentrations were not stable for the experimental run. Thus, we analyzed only the excerpt of the NO_3 data about the 4_1^0 band head. To compare our data to the CRD spectrum, we convoluted the OA-ICOS spectrum with a 0.1 cm^{-1} Gaussian line shape. The two spectra matched very well (Fig. 3.7).

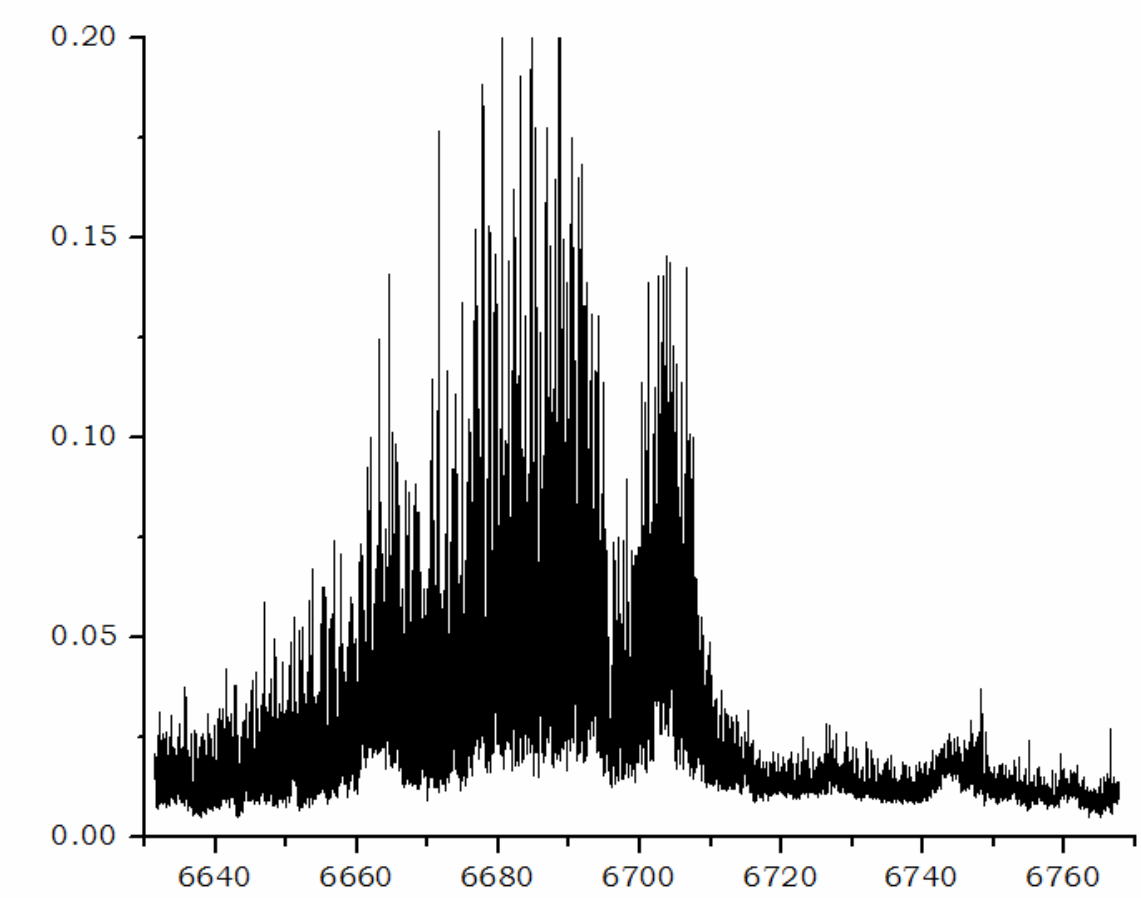

Figure A-3.18. Raw data from the OA-ICOS experiment (0.002 cm^{-1}). The bump at 6660 cm^{-1} is due to fluctuations in the NO_3 concentrations. For analysis, we therefore used only the 6680-6720 cm^{-1} region.

Appendix 3.7 References

(1) Jahn, H. A.; Teller, E. *Proc. R. Soc. Lond. A - Math. Phys. Sci.* **1937**, *161*, 220.
(2) Renner, R. *Z. Phys.* **1934**, *92*.
(3) Longuethiggins, H. C.; Opik, U.; Pryce, M. H. L.; Sack, R. A. *Proc. R. Soc. Lond. A - Math. Phys. Sci.* **1958**, *244*, 1.
(4) Opik, U.; Pryce, M. H. L. *Proc. R. Soc. Lond. A-Math. Phys. Sci.* **1957**, *238*, 425.
(5) Barckholtz, T. A.; Miller, T. A. *International Reviews in Physical Chemistry* **1998**, *17*, 435.
(6) Deev, A., *Ph. D. Thesis,* California Institute of Technology, 2004.
(7) Deev, A.; Sommar, J.; Okumura, M. *Journal of Chemical Physics* **2005**, *122*.
(8) Wayne, R. P.; Barnes, I.; Biggs, P.; Burrows, J. P.; Canosamas, C. E.; Hjorth, J.; Lebras, G.; Moortgat, G. K.; Perner, D.; Poulet, G.; Restelli, G.; Sidebottom, H. *Atmospheric Environment Part a - General Topics* **1991**, *25*, 1.
(9) Stanton, J. F.; Okumura, M. *Physical Chemistry Chemical Physics* **2009**, *11*, 4742.
(10) Donaldson, D. J.; Tuck, A. F.; Vaida, V. *Chemical Reviews* **2003**, *103*, 4717.
(11) Vaida, V. *Journal of Physical Chemistry A* **2009**, *113*, 5.
(12) Feierabend, K. J.; Havey, D. K.; Varner, M. E.; Stanton, J. F.; Vaida, V. *Journal of Chemical Physics* **2006**, *124*.
(13) Feierabend, K. J.; Havey, D. K.; Vaida, V. *Spectroc. Acta Pt. A - Molec. Biomolec. Spectr.* **2004**, *60*, 2775.
(14) Kawaguchi, K.; Shimizu, N.; Fujimori, R.; Tang, J.; Ishiwata, T.; Tanaka, I. *J. Molecular Spectroscopy* **2011 (submitted)**.
(15) Jacox, M. E.; Thompson, W. E. *Journal of Physical Chemistry A* **2009**, accepted.
(16) Bernath, P. *Spectra of Atoms and Molecules*; 2nd ed.; Oxford University Press: New York, 2005.
(17) Hirota, E.; Ishiwata, T.; Kawaguchi, K.; Fujitake, M.; Ohashi, N.; Tanaka, I. *Journal of Chemical Physics* **1997**, *107*, 2829.
(18) Herzberg, G. *Molecular Spectra and Molecular Structure (3 volume set)*; Krieger Pub., 1992.
(19) O'Keefe, A. *Chemical Physics Letters* **1998**, *293*, 331.
(20) Paul, J. B.; Lapson, L.; Anderson, J. G. *Applied Optics* **2001**, *40*, 4904.